JSS Focus Issue on Visible and Infrared Phosphor Research and Applications

Spectroscopy of Mn^{4+} in Double Perovskites, La_2LiSbO_6 and La_2MgTiO_6: Deep Red Photon Generators for Agriculture LEDs

A. M. Srivastava,[a,*,z] M. G. Brik,[b,c,d,*] H. A. Comanzo,[a] W. W. Beers,[e] W. E. Cohen,[e] and T. Pocock[f]

[a]*GE Global Research, One Research Circle, Niskayuna, New York 12309, USA*
[b]*College of Sciences, Chongqing University of Posts and Telecommunications, Chongqing 400065, People's Republic of China*
[c]*Institute of Physics, University of Tartu, Tartu 50411, Estonia*
[d]*Institute of Physics, Jan Dlugosz University, Armii Krajowej 13/15, PL-42200 Czestochowa, Poland*
[e]*Current & Lighting, Current Powered by GE, Cleveland, Ohio 44112, USA*
[f]*Lighting Enabled Systems & Applications ERC, Rensselaer Polytechnic Institute, Troy, New York 12180, USA*

The optical properties of Mn^{4+} ($3d^3$) in the double perovskites, La_2LiSbO_6 and La_2MgTiO_6, are investigated. The Mn^{4+} energy levels are calculated using the exchange charge model of crystal-field theory and compared with the experimental spectroscopic data. A comparative study of the optical properties of Mn^{4+} in the perovskite structure shows that energy of the $^2E_g \rightarrow {}^4A_{2g}$ emission transition is determined by octahedral site distortion. The greater is the site distortion, the lower is the Mn-O covalent interaction and the higher is the energy of the $^2E_g \rightarrow {}^4A_{2g}$ emission transition. The work provides guidelines for the development of deep red emitting phosphors for agricultural (horticultural) applications.
 [DOI: 10.1149/2.0191801jss]

Manuscript submitted July 25, 2017; revised manuscript received September 8, 2017. Published October 11, 2017. *This paper is part of the JSS Focus Issue on Visible and Infrared Phosphor Research and Applications.*

A phosphor emitting at wavelengths greater than 650 nm is not an efficient red photon generator for use in general illumination. This is because the spectrum of such phosphors will make a poor match with the human eye response (luminosity response function) resulting in low brightness even when the quantum efficiency of the phosphor is high. However, the far-red (FR) region (700–740 nm) of the spectrum generated by the deep red emitting phosphors has significant implications for plants. An important family of plant photoreceptors are the phytochromes (PHYs) that sense and signal changes in the red (660–670 nm) and FR (725–735 nm) ratios in a given spectrum.[1] Exposure of the plant to red light produces the biologically active PHY photoisomer (Pfr) while reversion to the inactive form (Pr) occurs under FR light.[2] They act as rapid and reversible molecular switches that can be used to control a wide variety of plant characteristics.[3] The balance of red to FR light is critical in nature and controlled environment agriculture as it regulates processes ranging from seed germination, height, leaf expansion, branching, plant immunity, circadian rhythm, leaf chlorophyll concentration to freezing tolerance.[4] Additionally, FR light plays a role in photosynthesis. The two photosystems (PSI and PSII) work electrochemically in series to generate the chemical energy required by the plant for growth and development. They absorb different regions of the spectrum with the quantum yields for PSII being greatest < 680 nm and is greatest between 680 nm and 720 nm for PSI.[5] In short, phosphors emitting wavelengths between 700–740 nm can be used to induce or inhibit photomorphogenesis (light mediated development) through PHYs in addition to optimizing photosynthesis through the balance of energy partitioning between the spectrally different photosystems.

A survey of the recent literature has indicated that research is being undertaken to device Mn^{4+} ($3d^3$ electronic configuration) based phosphors which in a phosphor coated LED lamp would emit deep red light for plant growth. Examples include Mn^{4+} activated La_2MgTiO_6,[6,7] La_2LiTaO_6,[8] La_2MgGeO_6,[9] Li_2MgZrO_4[10] and $Ca_{14}Zn_6(Al,Ga)_{10}O_{35}$.[11]

The compounds La_2MgTiO_6, La_2LiTaO_6 and La_2MgGeO_6 belong to the double perovskite family of compounds. We have extensively examined the optical properties of Mn^{4+} in ABO_3 and $A_2B^{'}B^{''}O_6$ compounds that crystallize in the perovskite structure. Examples include Gd_2MgTiO_6,[12] Ba_2LaNbO_6,[13] $NaLaMgTeO_6$,[14] $CaZrO_3$,[15] $LaAlO_3$,[16] $LaGaO_3$,[17] $GdAlO_3$,[18] $CaTiO_3$,[19] $YAlO_3$[20] and $SrTiO_3$.[21] The goal of our program is to develop a set of guidelines for tuning the wavelength of the $^2E_g \rightarrow {}^4A_{2g}$ emission transition, which per the Tanabe-Sugano diagram for d^3 ions, depends chiefly on the "Mn^{4+}-ligand" bonding covalence. Analysis of data presented in the archival literature reveals that the $^2E_g \rightarrow {}^4A_{2g}$ transition energy changes little in fluoride compounds and varies greatly in oxides.[22,23] This is because variation in covalence is smaller in fluorides than in oxides. Recently, we have presented how the "Mn^{4+}-ligand" covalent mixing is influenced by connectivity of the octahedral moieties and deviation of O-Mn-O bond angle from the ideal value of 90° in oxides.[24] We examined cases where the octahedral groups share corners (as in the ABO_3 and $A_2B^{'}B^{''}O_6$ perovskites) or edges and faces as in α-$LiAlO_2$, $Sr_4Al_{14}O_{25}$ and $CaAl_{12}O_{19}$.[24] It was concluded that a highly symmetrical octahedral moiety increases "Mn^{4+}-ligand" bonding covalence. The resulting emission spectrum is in the deep red because of the lowering of the $^2E_g \rightarrow {}^4A_{2g}$ emission transition energy.

Thus, a strategy for generating deep red photons in the perovskite structure for plant growth is to substitute Mn^{4+} in sites with near ideal O_h symmetry that maximizes "Mn^{4+}-ligand" bonding covalence. This can be achieved by choosing a perovskite lattice in which the corner linked octahedral groups with equal M-L bond lengths and O-M-O bond angles that do not deviate from the ideal values.

In this paper, we report the synthesis and spectroscopic properties of the double perovskite La_2LiSbO_6 activated with Mn^{4+}. For comparative purposes, we also evaluate the spectroscopic data of the double perovskite, La_2MgTiO_6:Mn^{4+}, which has been reported in the literature.[6,7] For both compounds, the energy position of the Mn^{4+} $^2E_g \rightarrow {}^4A_{2g}$ emission transition is identified and electronic energy levels calculated using the exchange charge model of crystal-field theory. This work is consistent with our goal of connecting the Mn^{4+} emission wavelength with structural peculiarities that control the covalence of "Mn^{4+}-ligand" bonding.

Experimental

The compound $La_2Li(Sb_{0.998}Mn_{0.002})O_6$ was synthesized by a conventional solid-state reaction technique. Prior to its use as the starting

*Electrochemical Society Member.
[z]E-mail: srivastava@ge.com

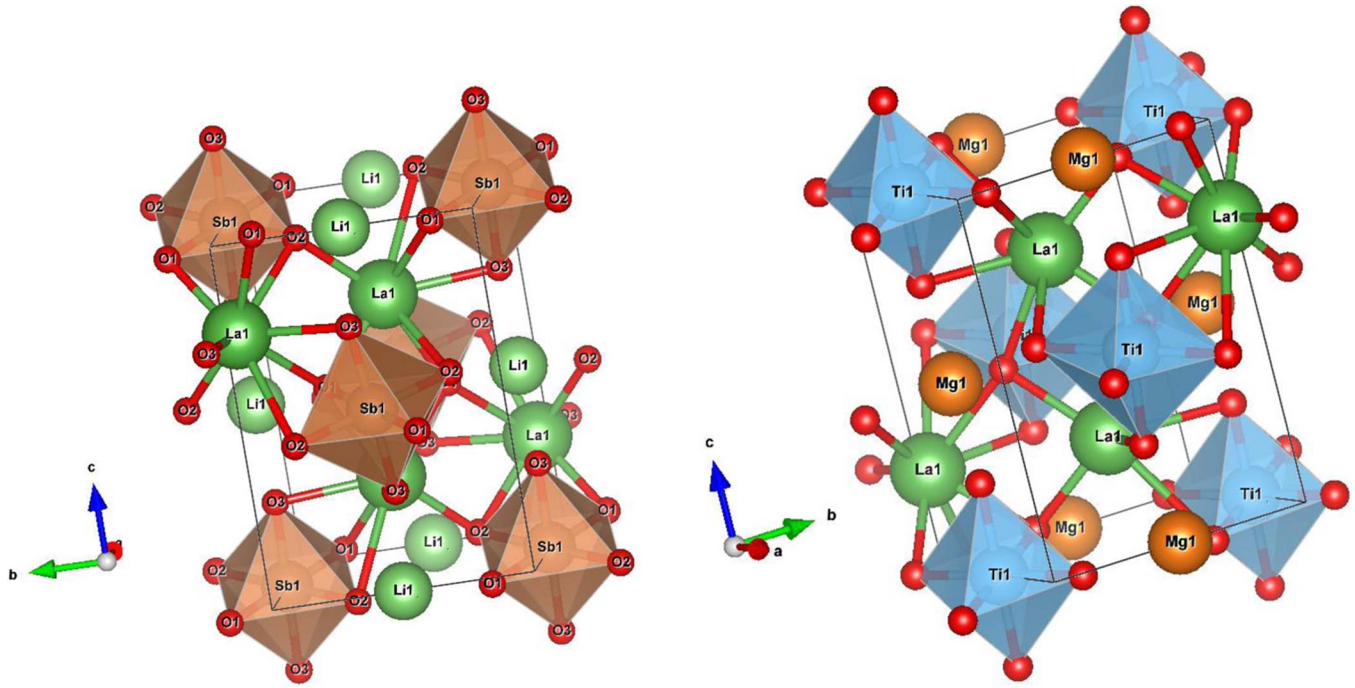

Figure 1. One unit cells of La_2LiSbO_6 (left) and La_2MgTiO_6 (right). Drawn with VESTA.[28] The octahedral coordination of the Sb and Ti ions and chemical bonds around La ions are shown.

material, La_2O_3 (Alfa Aesar, 99.99%) was heated to 1000°C under nitrogen atmosphere. An excess (50 mole% over the stoichiometric proportion) of the starting material Li_2CO_3 (Alfa Aesar, 99.998%) was added to compensate for any loss of lithium occurring because of the high vapor pressure at high temperatures during synthesis. These starting materials were blended with Sb_2O_3 (Alfa Aesar, 99.9%) and Mn_2O_3 (Aldrich 99.999%) and heated in air at 700°C for one hour. The resulted powder was ball milled and heated to 1000°C for 10 h to form the final product.

Luminescence measurements were performed as previously described.[12] The spectra were corrected for the wavelength dependent variations in the Xe-lamp intensity and the photomultiplier response.

Crystal Structure of La_2LiSbO_6 and La_2MgTiO_6 and Method of Calculations

Structural studies on La_2LiSbO_6 are presented in References 25,26. The compound crystallizes in the $P2_1/C$ space group (No. 14) with two formula units per unit cell. The lattice constants are (in Å): a = 5.6226, b = 5.7199, c = 7.9689, β = 89.796°

In Reference 6, the XRD pattern of La_2MgTiO_6 is indexed on a cubic cell. However, the monoclinc $P2_1/n$ space group is better suited to explain the diffraction pattern of this perovskite.[27] For our analysis, the data presented in Reference 27 where the XRD pattern is indexed on a monoclinc cell is used. The double perovskite crystallizes in the $P2_1/C$ space group (No. 14) with four formula units per unit cell. The lattice constants are (in Å): a = 5.5467, b = 5.5616, c = 7.8426, β = 89.959°.[27]

In these perovskites, the Mn^{4+} ions substitute for the six-fold coordinated Sb^{5+} and Ti^{4+} ions, respectively. Obviously, in La_2LiSbO_6 charge-compensation is required when Mn^{4+} replaces Sb^{5+} in the lattice. The La^{3+} ions in both cases are eight-fold coordinated, and the Li^+, Mg^{2+} ions are six-fold coordinated (Figure 1). Enlarged views of the TiO_6 and SbO_6 octahedral complexes along with bond lengths and bond angles are shown in Fig. 2.

Details pertaining to the calculations of the Mn^{4+} energy level by the exchange charge mode of crystal field theory has been presented before.[29,30,31] The reliability and vitality of the ECM is confirmed by its success in calculating the energy level of the transition metal and rare earth ions.[30,31] and references therein In the following we will only provide the results of our calculations that are relevant to the interpretation of the La_2LiSbO_6:Mn^{4+} and La_2MgTiO_6:Mn^{4+} experimental spectra.

Results and Discussion

X-ray diffraction pattern of $La_2Li(Sb_{0.998}Mn_{0.002})O_6$.—Apart from very weak lines which were identified as being caused by the minor phase of Li_3SbO_4, the X-ray diffraction pattern of the $La_2Li(Sb_{0.998}Mn_{0.002})O_6$ product indicated a single-phase material with monoclinic symmetry.

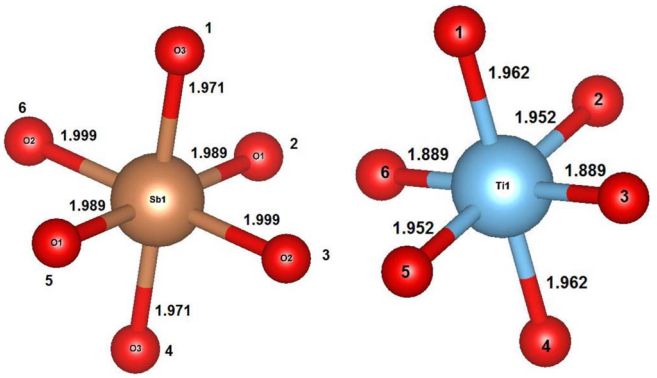

Figure 2. Enlarged views of the SbO_6 (left) and TiO_6 (right) complexes in La_2LiSbO_6 and La_2MgTiO_6. Drawn with VESTA.[29] The chemical bond lengths (in Å) are shown. All characteristic angles (in °) are listed below for each complex. SbO_6: 1-Sb1-4, 2-Sb1-5, 3-Sb1-6 – 180; 1-Sb1-2, -3, -5, -6: 89.97, 89.28, 90.03, 90.72, correspondingly; 2-Sb1-3, -4, -6: 91.94, 90.03, 88.06; 3-Sb1-4, -5: 90.72, 88.06; 4-Sb1-5, -6: 89.97, 89.28; 5-Sb1-6: 91.94. TiO_6: 1-Ti1-4, 2-Ti1-5, 3-Ti1-6 -180; 1-Ti1-2, -3, -5, -6: 86.74, 89.42, 93.26, 90.58, correspondingly; 2-Ti1-3, -4, -6: 94.91, 93.26, 85.09; 3-Ti1-4, -5: 90.58, 85.09; 4-Ti1-5, -6: 86.74, 89.42; 5-Ti1-6: 94.91.

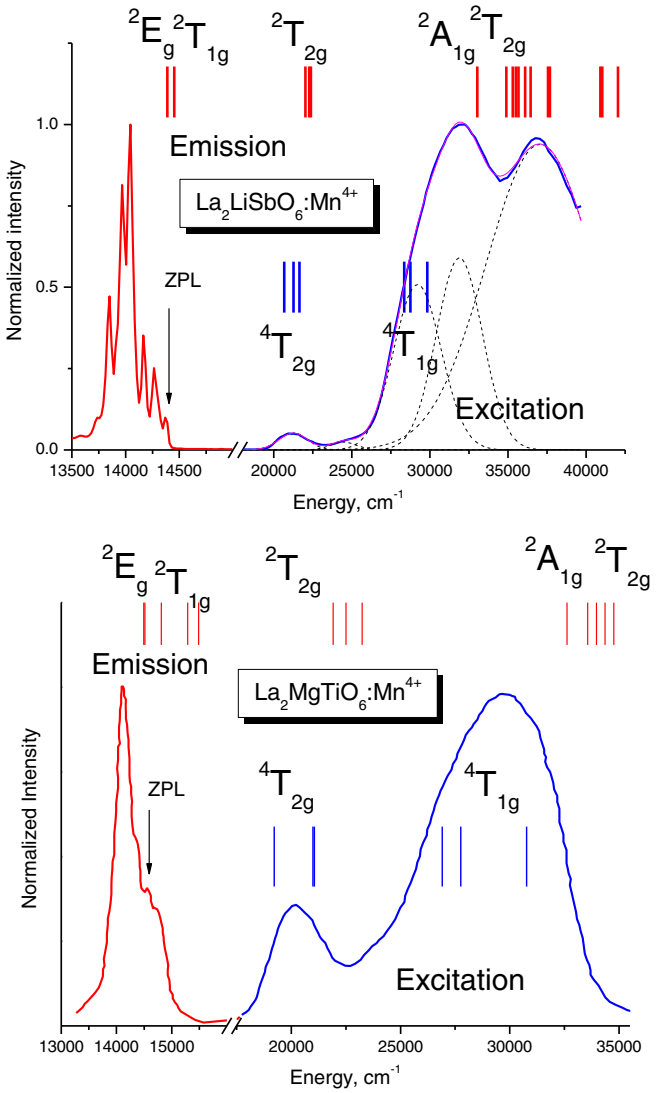

Figure 3. Comparison of the experimental emission and excitation spectra with the calculated energy levels of Mn^{4+} in La_2LiSbO_6 [T = 10 K] and La_2MgTiO_6.[6] Decomposition of the excitation band in La_2LiSbO_6 into Gaussian components is shown. This permits the proper location of the $^4T_{1g}$ level.

Spectroscopic properties of $La_2Li(Sb_{0.998}Mn_{0.002})O_6$ and $La_2MgTiO_6:Mn^{4+}$.—Fig. 3 exhibits the low temperature excitation and emission spectra of $La_2Li(Sb_{0.998}Mn_{0.002})O_6$ (T = 10 K). At this temperature, the emission spectrum is composed of the zero-phonon line at 695 nm (14 388 cm^{-1};$^2E_g \rightarrow {}^4A_{2g}$) and the Stokes vibronic bands at 706 nm (14 164 cm^{-1}), 713 nm/716 nm (14 025 cm^{-1}/13 966 cm$^{\mp 1}$) and 722 nm/729 nm (13 850 cm^{-1}/13 717 cm^{-1}). The Stokes bands can be assigned to the ungerade modes of the MnO_6 octahedral moiety: ν_6 = 224 cm^{-1}, ν_4 = 363 cm^{-1} and 422 cm^{-1}, ν_3 = 538 cm^{-1} and 671 cm^{-1}. The strong line at 123 cm^{-1} from the ZPL is an external (lattice) mode. At higher temperatures, the anti-stokes lines appear on the high frequency side of the ZPL.

The excitation spectrum was decomposed into a sum of Gaussian to identify the energy positions of the various transitions (Fig. 3). This was necessary because the overlap of $O^{2-} \rightarrow Mn^{4+}$ charge transfer and $^4A_{2g} \rightarrow {}^4T_{1g}$ transitions makes the positing of the $^4T_{1g}$ excitation band difficult. The band in the excitation spectrum at 37 050 cm^{-1} (270 nm) is assigned to the host lattice absorption. Excitation bands at 31 870 cm^{-1} (314 nm), 29 180 cm^{-1} (342 nm) and 21 240 cm^{-1} (470 nm) correspond with the $O^{2-} \rightarrow Mn^{4+}$ charge transfer, $^4A_{2g} \rightarrow {}^4T_{1g}$ and $^4A_{2g} \rightarrow {}^4T_{2g}$ transitions, respectively.

Table I. The crystal field (Stevens normalization) and Racah parameters (all in cm^{-1}) for Mn^{4+} ions in La_2LiSbO_6 and La_2MgTiO_6.

	La_2LiSbO_6	La_2MgTiO_6
B_2^{-2}	172	3452
B_2^{-1}	618	4661
B_2^0	725	−1025
B_2^1	−1856	−5901
B_2^2	1486	4982
B_4^{-4}	−16646	12081
B_4^{-3}	−14195	−5572
B_4^{-2}	1833	−3387
B_4^{-1}	−5643	−4341
B_4^0	4002	3958
B_4^1	−24188	21633
B_4^2	2360	352
B_4^3	−23385	24765
B_4^4	−19400	−23641
B	750	700
C	2953	3136

The spectroscopic properties of Mn^{4+} in the double perovskite La_2MgTiO_6 were taken from Reference 6. The low temperature (T = 10 K) emission spectrum locates the $^2E_g \rightarrow {}^4A_{2g}$ emission transition at 690 nm (14 493 cm^{-1}).[7]

We wish to point out that the emission spectra of the two perovskites (Fig. 3) are in the 700–740 nm wavelength range that is important for the plant growth application (see Introduction).

Results of energy level calculations.—The octahedral moieties in both La_2LiSbO_6 and La_2MgTiO_6 deviate considerably from the ideal O_h group. As exhibited in Fig. 2, both octahedral clusters are characterized by the presence of three pairs of different interatomic distances. Further, the characteristic octahedral bond angles are also deviating from the ideal values. Therefore, all orbitally degenerated energy levels of the Mn^{4+} ion in such clusters will be split.

The crystal structural data were used to calculate the non-zero parameters of crystal field, which are listed in Table I. The values of the Racah parameters B and C, which were chosen from the best agreement with experimental data, are also given in Table I. We should point out that the value of the second Racah parameter C is found from adjusting the calculated position of the ^2E_g (^2G) state to its experimental value determined from the emission spectrum. Thus, it is imperative to correctly identify the energy position of the $^2E_g \rightarrow {}^4A_{2g}$, zero phonon transition.

The crystal field splitting of all 8 LS terms of the Mn^{4+} ion was calculated by diagonalizing the crystal field Hamiltonian with all crystal field parameters. The lowest calculated energy levels, which are located in the spectral range corresponding to the experimental excitation/emission spectra, are listed in Table II. The low symmetry of the crystal lattice sites is confirmed by a complete removal of the orbital degeneracy of the triplet and doublet states. There is good agreement between these calculated energy levels and corresponding experimental spectra (Fig. 3). Note that the splitting of the orbital triplets in La_2MgTiO_6 is greater than in La_2LiSbO_6, which indicates considerably lower crystal field symmetry in the former case.

Influence of MnO_6 distortions on the energy of the ^2E_g state in double perovskites.—In this section, we present a comparative study of the spectroscopic properties of Mn^{4+} ion in double perovskite compounds with the formulation $A_2BB'O_6$ (Table III). The study establishes a relationship between the energy position of the ^2E_g state and octahedral site distortion. The greater is the octahedral distortion,

Table II. Calculated energy levels (in cm^{-1}) for Mn^{4+} in La_2LiSbO_6 and La_2MgTiO_6.

	La_2LiSbO_6	La_2MgTiO_6
$^4A_{2g}$ (^4F)	0	0
^2E_g (^2G)	14387, 14453	14492, 14514
$^2T_{1g}$ (^2G)	15020, 15100, 15171	14811, 15288, 15487
$^4T_{2g}$ (^4F)	20666, 21255, 21640	19214, 20992, 21054
$^2T_{2g}$ (^2G)	22018, 22267, 22368	21920, 22499, 23243
$^4T_{1g}$ (^4F)	28358, 28752, 29836	26906, 27754, 30770
$^2A_{1g}$ (^2G)	33032	32619
$^2T_{2g}$ (^2H)	34898, 35305, 35502	33560, 33971, 34360
$^4T_{1g}$ (^4P)	45412, 45994, 46600	42823, 45413, 46787

the smaller is the overlap between the Mn and O wave functions and higher is the energy position of the ^2E_g state.

In Table III compares the values for the Racah parameters B and C, peak emission energy of the $^2E_g \rightarrow {}^4A_{2g}$ transition and the value of the non-dimensional quantity $\beta_1 = \sqrt{(\frac{B}{B_0})^2 + (\frac{C}{C_0})^2}$, (the subscript "0" refers to the values of the Racah parameters of the free ion) for Mn^{4+} in three double perovskites and in $SrTiO_3$. The function β_1 was introduced by Brik and Srivastava[16] in the spectroscopy of d^3 ions to connect the energy of the $^2E_g \rightarrow {}^4A_{2g}$ transition with the Racah parameters B and C.

In an ideal octahedral moiety, all six bonds are equal. Out of 15 characteristic angles of an octahedron, three are 180° and twelve are 90°. There are two ways in which the octahedral moiety of the perovskite lattice can distort: varying M-O interatomic distances and the O-M-O bond angle deviating from the ideal 90° value.

The data in Table III are arranged in the order of decreasing octahedral distortions as deduced from the crystallographic data of each compound. We start with the double perovskite, Ba_2LaNbO_6 in which the ^2E_g state is located at the highest energy (14 992 cm^{-1}). In this perovskite, the O-Nb-O bond angle deviates from 90° by about 8° and the linear O-Nb-O bond angle is very nearly 180°.[13,32]

In La_2MgTiO_6, the TiO_6 moiety is more regular; the O-Ti-O bond angle is deviating from 90° by about 4.9°. The linear O-Nb-O bond angle is very nearly 180°. The smaller angular deviation from 90° increases Mn-O covalent interaction and results in a lower energy of the ^2E_g (14 492 cm^{-1}).

In the family of double perovskites, the lowest energy of the ^2E_g state is found in La_2LiSbO_6 (Table III). In this perovskite, the SbO_6 octahedral group is comparatively very symmetrical; the linear O-Sb-O bond angle is 180° and the deviation from 90° is <1°. The increased Mn-O covalent interaction results in the ^2E_g state being located at lower energy, 14 388 cm^{-1}.

Finally, for comparative purposes, we consider the $SrTiO_3$ perovskite in which the ^2E_g state is located at very low energy (13 792 cm^{-1}). In this perovskite, the octahedral moieties are perfectly symmetrical: O-Mn-O bond angles are the ideal 90° and 180° and all Ti-O bond lengths are equal (1.951 Å). Therefore, there is a strong covalent bonding between the Mn and the six oxygen neighbors which decreases the energy of the ^2E_g state.

Figure 4 shows that energy of the $^2E_g \rightarrow {}^4A_{2g}$ emission transition is linearly related to the β_1 parameter. Further, the β_1 parameter reflect correctly the bonding covalence variation in these perovskites as deduced from the magnitude of octahedral site distortion. Therefore, oxide perovskite lattice in which the O-Mn-O bond angles do not deviate much from the ideal 180° and 90° values and in which the Mn-O bond lengths are equal are ideally suited for the development of deep red emitting phosphors for plant growth application.

Table III. The Racah parameters (B, C), $\beta_1$and the energy of the $^2E_g \rightarrow {}^4A_{2g}$ emission transition (E:^2E_g) in double perovskites and in $SrTiO_3$.

Phosphor	B (cm^{-1})	C (cm^{-1})	β_1	E:^2E_g (cm^{-1})	Reference
Ba_2LaNbO_6	670	3290	0.956	14992	13,32
La_2MgTiO_6	700	3136	0.944	14492	This work[6,7]
La_2LiSbO_6	750	2953	0.94	14388	This work
$SrTiO_3$	735	2812	0.91	13792	21

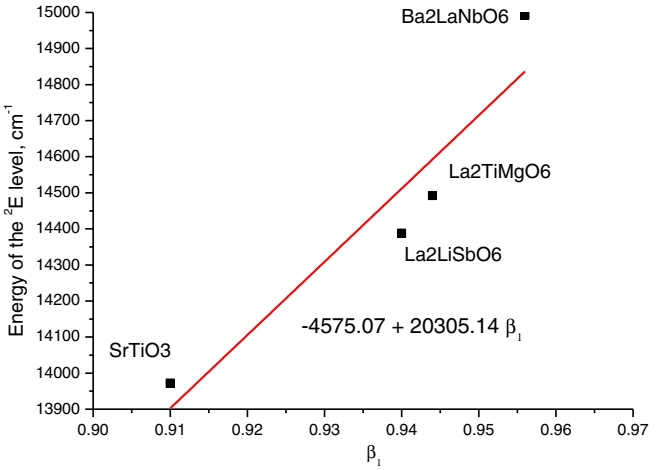

Figure 4. The relationship between the energy of the ^2E_g state and the β_1 parameter.

LED Horticultural Market

The WinterGreen Research "LED Grow Light Market Shares, Strategies, and Forecast Worldwide" report projects the horticultural market at $3.6 billion by 2020.[33] A key factor driving the large-scale adoption of this technology is energy savings and the use of LEDs to control and improve crop production. Such market data will continue to motivate the search for phosphors that enable spectrally tailored LEDs for horticultural applications.

Conclusions

The energy levels of Mn^{4+} in the double perovskites La_2LiSbO_6 and La_2MgTiO_6 are calculated by the exchange charge model of crystal field that allows to calculate the crystal field parameters and splitting of the orbitally degenerated energy levels. Agreement between the calculated and experimental results was shown to be good. Our study shows that octahedral site distortions decreases Mn-O covalent interaction which increases the energy of the ^2E_g state. We, therefore, conclude that the development of deep red emitting phosphors for plant growth application in the perovskite based materials requires minimization of the octahedral site distortion. This results in stronger Mn-O covalent bonding interaction which decreases the energy of the Mn^{4+} $^2E_g \rightarrow {}^4A_{2g}$, zero phonon transition.

Acknowledgments

M. G. Brik thanks the supports from the Recruitment Program of High-end Foreign Experts (grant No. GDW20145200225), the Programme for the Foreign Experts offered by Chongqing University of Posts and Telecommunications, Ministry of Education and Research of Estonia, Project PUT430, and European Regional Development Fund (TK141).

References

1. T. Pocock, *HortScience*, **50**, 1281 (2015).
2. K. Franklin and P. Quail, *Journal of Experimental Botany.*, **61**, 11 (2010).
3. H. Smith and C. G. Whitelam, *Plant and Cell Environment*, **20**, 840 (1997).
4. T. Pocock, in *Light Emitting Diodes for Agriculture-Smart Lighting.*, Ghupta Dutta, Editor, Springer. In press. (2017).

5. A. Laisk, V. Oja, H. Eichelmann, and L Dall'Osto, *Biochimica et Biophysica Acta.*, **1837**, 315 (2014).
6. Ziwei Zhou, Jiming Zheng, Rui Shi, Niumiao Zhang, Jiayu Chen, Ruoyu Zhang, Hao Suo, Ewa M. Goldys, and Chongfeng Guo, *ACS Appl. Mater. Interfaces*, **9**, 6177 (2017).
7. Yohei Takeda, Hideki Kato, Makoto Kobayashi, Hisayoshi Kobayashi, and Masato Kakihana, *Chem. Lett.*, **44**, 1541 (2015).
8. Lei Wang, Lin Yuan, Yudong Xu, Rulong Zhou, BingYan Qu, Ning Ding, Min Shi, Bo Zhang, Yiqing Chen, Yang Jiang, Di Wang, and Junyan Shi, *Applied Phys.*, **A117**, 1777 (2014)
9. Mizuki Watanabe, Tsubasa Yoshizawa, Sun Woog Kim, Kohei Seki, Tadashi Ishigaki, Kazuyoshi Uematsu, Kenji Toda, and Mineo Sato, *ECS Meeting Abstract*, Abstract **2016** MA2016-02 3192, JO2 Poster Session-Oct 4 2016.
10. R. Cao, Z. Shi, G. Quan, T. Chen, S. Gao, Z. Hu, and P. Liu, *J. Lumin.*, **188**, 577 (2017).
11. Kohei Seki, Kazuyoshi Uematsu, Kenji Toda, and Mineo Sato, *Chem. Lett.*, **43**, 1213 (2014).
12. A. M. Srivastava and W. W. Beers, *J. Electrochem. Soc.*, **143**, L203 (1996).
13. A. M. Srivastava and M. G. Brik, *J. Lumin.*, **132**, 579 (2012) 579.
14. Alok M. Srivastava, M. G. Brik, Samuel. J. Camardello, Holly. A. Comanzo, and Florencio Garcia-Santamaria, *Zeitschrift fuer Naturforschung*, **69b**, 1 (2014).
15. M. G. Brik and A. M. Srivastava, *ECS Journal of Solid State Science and Technology*, **2** R1 (2013).
16. A. M. Srivastava and M. G. Brik, *Opt. Mat.*, **35**, 1544 (2013).
17. A. M. Srivastava, S. J. Camardello, and M. G. Brik, *J. Lumin.*, **183**, 437 (2017)
18. A. M. Srivastava and M. G. Brik, *Opt. Mat.*, **63**, 207 (2017)
19. Vesna Dordevic, Mikhail G. Brik, Alok M Srivastava, Mina Medic, Predrag Vulic, Estelle Glais, Bruno Viana, and Miroslav D Dramicanin, *Optical Materials*, accepted.
20. M. G. Brik, I. Sildos, M. Berkowski, and A. Suchocki, *J. Phys.: Condens. Matter.*, **21**, 025404 (2009).
21. M. G. Brik and N. M. Avram, *J. Phys.: Condens. Matter.*, **21**, 155502 (2009).
22. M. G. Brik and A. M. Srivastava, *J. Lumin.*, **133**, 69 (2013).
23. M. G. Brik, S. J. Camardello, and A. M. Srivastava, *ECS Journal of Solid State Science and Technology*, **4**, R39 (2015).
24. A. M. Srivastava and M. G. Brik, *ECS Journal of Solid State Science and Technology*, accepted (2017).
25. M. L. Lopez, J. Isasi, I. Alvarez, M. L. Veiga, and C. Pico, *Anales de Qimica*, **87**, 959 (1991).
26. M. L. Lopez, M. L. Veiga, J. Rodriguez-Carvajal, F. Fernandez, A. Jerez, and C. Pico, *Mater. Res. Bull.*, **27**, 647 (1992).
27. D. Y. Lee, S.-J. Yoon, J. H. Yeo, S. Nahm, J. H. Paik, K.-C. Whang, and B. G. Ahn, *J. Mater. Sci. Lett.*, **19**, 131 (2000).
28. K. Momma and F. Izumi, *J. Appl. Crystallogr.*, **44** 1272 (2011).
29. M. G. Brik, A. M. Srivastava, and N. M. Avram, *J. Lumin.*, **131**, 54 (2011).
30. B. Z. Malkin, in *Spectroscopy of solids containing rare-earth ions*, A. A. Kaplyanskii and B.M. Macfarlane, Editors, p. 13, North-Holland, Amsterdam, 1987.
31. Nicolae M. Avram and Mikhail G. Brik, Editors, *Optical Properties of 3d-Ions in Crystals: Spectroscopy and Crystal Field Analysis, Editors*, Springer and Tsinghua University Press, (2013).
32. Peter A. Tanner and Zaifa Pan, *Inorg. Chem.*, **48** 11142 (2008).
33. http://www.ledsmagazine.com/articles/print/volume-12/issue-3/features/life-science/led-technology-serves-rapidly-growing-horticultural-market.html